

Submarine lidar for seafloor inspection

Stefan Harsdorf†, Manfred Janssen†, Rainer Reuter†,
Stefan Toeneboen†, Bernhard Wachowicz† and Rainer Willkomm‡

† Physics Department, Marine Physics Group, Universität Oldenburg, 26111 Oldenburg, Germany

‡ TriOS Optical Sensors, Werftweg 15, 26135 Oldenburg, Germany

Received 2 August 1999, in final form and accepted for publication 5 October 1999

Abstract. Substances released at sea by accident or illegal discharges are characterized by a broad range of chemical and physical properties. Moreover, the characteristics of coastal waters, e.g. in the German Bight, are highly variable. Due to this a submersible sensor network for the detection of hazardous substances on the seafloor combining several instruments based on different physical and chemical principles has been under development since 1996. In addition to conventional sensors for seawater analysis and seafloor monitoring such as CTD probes (conductivity, temperature, depth) and video cameras, the system includes several newly developed instruments for the detection of dissolved and sunken pollutants.

One of these instruments is the submarine lidar, combining a range-gated imaging device and a fluorescence lidar. A *q*-switched Nd:YAG laser is used as the common light source. Applying the expanded frequency-doubled laser pulse the gated CCD camera is particularly useful for recording images of damaged containers with chemical cargo where harmful substances might be released into the water column. Tuned to UV emission, the same laser is used for remotely classifying fluorescent substances spreading on the seafloor.

The intention of this paper is to present the submarine lidar in detail and to give an overview of its physics and potential applications.

Keywords: fluorescence lidar, range-gating video, seafloor monitoring

1. Submarine sensor network for pollution monitoring in the German Bight

Hamburg harbour and the channel between the North Sea and the Baltic Sea, the gateway to Eastern Europe and Scandinavia, make the German Bight a coastal zone with one of the highest levels of ship traffic in the world. Although a complex and comprehensive surveillance system has been installed by the littoral states, ship accidents cannot be completely precluded, and harmful substances may enter the sea, seeping out at the bottom from leaks of damaged containers. Table 1 lists four examples of high density and insoluble materials which are transported.

However, fast detection, localization and identification of lost cargo and toxic chemicals in the sea are necessary to protect the environment and people. To ensure efficient recovery the German Ministry of Transport intends to operate a submersible sensor network aboard the multipurpose vessel 'Neuwerk'. Because of the vast number of possible scenarios, the network consists of several sensors using various chemical and physical principles. It will be integrated into a specially adapted frame or later into the payload of an ROV (remotely operated vehicle). In addition to basic sensors such as underwater video cameras and probes for measuring seawater temperature, conductivity and pH, the

Table 1. Insoluble chemicals and their transport rates in German harbours during 1984 [1].

Substance	Density	Annual transport rate
Benzyl chloride	1.105 g cm ⁻³	3 750 t a ⁻¹
Chlorobenzene	1.106 g cm ⁻³	15 000 t a ⁻¹
Ethylene dichloride	1.253 g cm ⁻³	220 000 t a ⁻¹
1,1,1-trichloroethane	1.338 g cm ⁻³	57 500 t a ⁻¹

payload includes several newly developed instruments [2]:

- a lidar for inspecting the seafloor, which combines a range-gated video device with a time-resolved fluorometer (University of Oldenburg, Laser Remote Sensing Group),
- an acoustic sensor for measuring the acoustic impedance of the seafloor/water column interface (University of Oldenburg, Acoustics Group),
- a membrane induction/gas chromatograph/mass spectrometer (Technical University of Hamburg–Harburg), and
- a quartz microbalance sensor array (University of Magdeburg/RST Rostock).

Prototypes of these sensors have been realized and successfully operated within the frame of the submersible

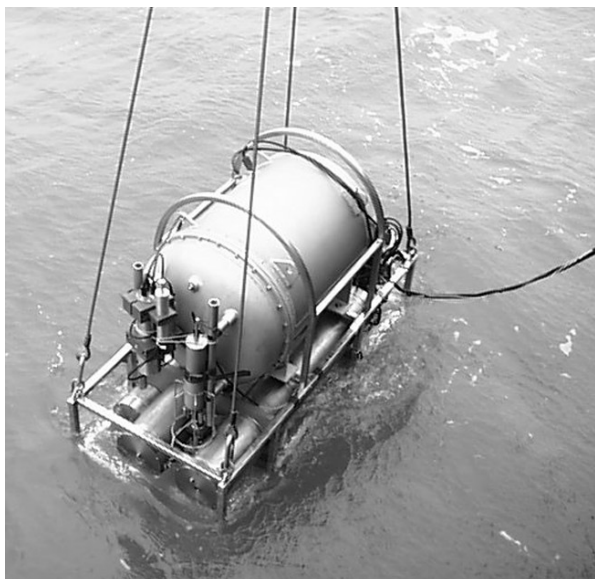


Figure 1. Sensor network aboard the RV Heincke in May 1999.

sensor network during a first sea trial aboard the RV Heincke (figure 1). Data transfer to the operator and data analysis in real time are realized. To enable a fast and efficient data interpretation, instruments and control unit form an ethernet network. The central computer aboard the multipurpose vessel is connected to the sensors in the payload frame for instrument control and data acquisition. The central computer is also connected to a database of chemical pollutants and a mass storage device which allows for a joint data analysis and interpretation. Combined data acquisition and interpretation is realized by specially adapted software which provides more information than a simultaneous operation of different instruments. The system is handled like a single instrument. It forms an open frame structure with well-defined mechanical, electrical and software interfaces to allow for an easy installation of other sensors in the future, including integration with other existing surveillance systems.

2. Submarine lidar

2.1. Method

Most of the conventional sensors analyse seawater *in situ* to measure dissolved chemicals. Packaged cargo and insoluble chemicals with a density $> 1 \text{ g cm}^{-3}$ on the seafloor cannot be located. Standard video cameras are also often unsuitable for seafloor imaging because of the high turbidity in the German Bight. Further, pools of sunken chemicals on the sediment can hardly be seen on video images taken from above. In particular, on coarse-grained sediment the contour of a sinker bubble adapts to the ground so that the low gradient of the index of refraction usually does not provide sufficient contrast in such images.

The submarine lidar is a combination of a range-gated video device and a time-resolved fluorescence lidar. Range-gated imaging is a well known technique to enhance the performance of underwater video cameras. In accordance

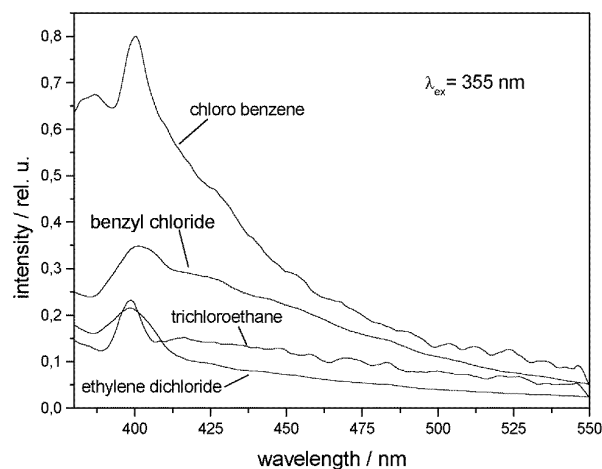


Figure 2. Emission spectra for excitation wavelength 355 nm.

with the concept of lidar a short laser pulse is used as the illumination source for a camera with an exposure time in the range of a few nanoseconds. A synchronization of laser emission and camera gate-on time allows one to suppress the backscattered light from the water column between detector and object, and to record only the light backscattered by the object. This generally results in a contrast-enhanced video image. The gated camera of the submarine lidar is used to look for and in the case of success to inspect sunken cargo. Upon detection of an object, the fluorescence lidar is applied to record signals from substances within the water column and on the seafloor which are invisible on the scattered light images. Analysis of emission spectra allows one to distinguish between natural substances, e.g. yellow substance and pollutants. Figure 2 shows the emission spectra of the substances listed in table 1. Spectra are excited at 355 nm and measured with a laboratory fluorometer.

Additionally, visual information from the range-gated video device are needed in order to interpret the fluorescence measurements in a correct and efficient way.

The application of lidar techniques which are very well investigated in the air allows the visualization of fluorescent chemicals on the seafloor without any damage to the ecosystem. An altitude of a few metres above ground prevents sediment from rising and reducing visibility. Contamination of the system is largely avoided.

Due to the fact that signals are transmitted through the water column the performance of the underwater lidar is limited to low and medium turbid waters.

2.2. Instrument layout

The integration of the lidar into the payload of an ROV and underwater operation lead to high demands on its technical layout, e.g. mass and power consumption have to be minimized.

The housing of the lidar is made of two titanium cylinders, each with a diameter of 220 mm and a length of 1340 mm. One cylinder contains the Nd:YAG laser as the light source of the instrument; the video camera and the detection unit of the fluorescence lidar are integrated in the second cylinder. Interfaces for the excitation and detection

of signals are quartz windows. Electromagnetic interference produced by the pulse laser is very critical since it might degrade the quality of small lidar signals. The concept of using separate cylinders for the laser and the detector assembly, which is most sensitive to interference, reduces this disturbance.

A Nd:YAG laser is applied as the light source of the instrument. It provides its second harmonic laser pulse at 532 nm which allows a maximum penetration depth, and its third harmonic laser pulse at 355 nm is a good compromise between effective excitation of fluorescence and good transmission through the water column. The laser has 160 mJ pulse energy at 532 nm and 60 mJ at 355 nm, and 4 ns pulse duration. Three illumination modes are realized by the use of tilting mirrors: UV emission as the light source of the fluorescence lidar, the beam expanded green emission for illumination of the seafloor when taking video images, and the expanded UV emission to maintain the possibility of fluorescence imaging. The divergence of the expanded beams is adapted to the camera field of view. The final definition of the field of view angle will be based on experience gained during continuous operation.

Video images are taken with a gateable intensified CCD camera with 520×736 pixels and 8 bit resolution. Its minimum gate-on time is 5 ns. The maximum image repetition frequency is 20 Hz. Gate and delay time are adjustable in steps of 1 ns.

Fluorescence can be measured from small spots on the ground at positions that can be selected with a two-dimensional optical scanner. The receiver consists of a telescope with 50 mm free aperture, optical filters to block the reflected laser pulse and to select the detection wavelength, a fast photomultiplier and a PC card transient recorder with 500 MHz sampling rate and 8 bit resolution. Wavelength selection is done with a filter wheel, equipped with a semi-circular variable interference filter for the 400–700 nm range with a medium half-width of 15 nm and four interference filters for the 355–400 nm range. An 80 dB high-speed logarithmic amplifier compresses the photomultiplier signals before digitization to enhance the dynamic range. Four different high voltages for the photomultiplier are remotely selectable, and a shutter is situated in front of its diaphragm.

Additional parameters like roll angle, pitch angle, pressure corresponding to depth, humidity inside both tubes and temperature of the cooling-water circuit are measured continuously.

A miniaturized PC controls the illumination modes, operates the transient recorder and the CCD camera, and organizes the data transfer between the instrument and the deck unit on board the ship.

2.3. Theory and data interpretation

2.3.1. Range-gated scattered light imaging. An image which has been recorded underwater can be regarded as a superposition of three components [3]:

$$E_{\text{total}} = E_{\text{direct}} + E_{\text{forward}} + E_{\text{back}}. \quad (1)$$

The total irradiance in the image plane is E_{total} . The irradiance due to photons which are scattered by an object and

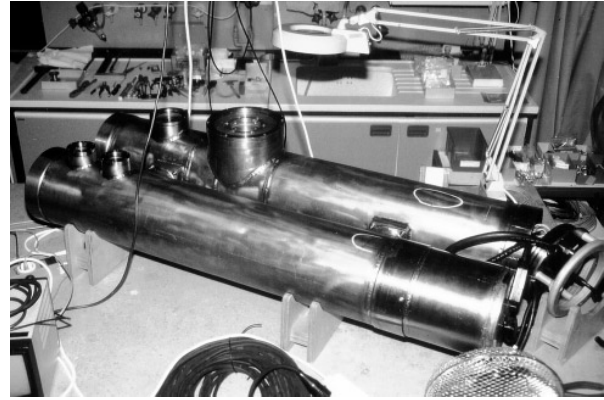


Figure 3. Submarine lidar housing including the cooling unit.

returned to the camera without any interaction with the water is denoted by E_{direct} . The part which has been scattered by the object and again forward scattered in a small angle within the water column before being recorded by the camera is E_{forward} . Finally, the photons which have been backscattered in the water and hit the camera without having reached the object correspond to E_{back} . The components E_{direct} and E_{forward} contain information about the object in contrast with E_{back} which is completely independent of the object. Range gating is based on the temporal fade-out of backscattering from the water. The irradiance in a range-gated image can therefore be given in a first approximation by

$$E_{\text{total_rg}} = E_{\text{direct}} + E_{\text{forward}}. \quad (2)$$

In general, the radiance emitted by a point within the object plane can be regarded as Lambert distributed. The relation between $E_{\text{total_rg}}$ and the irradiance E_{object} of the object is given by the point spread function (psf):

$$\begin{aligned} E_{\text{total_rg}}(x, y) &= \iint \text{psf}(x - x', y - y', R) \cdot E_{\text{object}}(x', y') \cdot dx' dy' \\ &= \text{psf} \otimes E_{\text{object}}. \end{aligned} \quad (3)$$

The symbol for convolution is \otimes . The psf characterizes scattering effects of the image transfer through a turbid medium and is responsible for the blur of the image. Equation (3) implies that, if the psf is known, an underwater image can be restored using numerical image reconstruction techniques, e.g. the Richardson–Lucy algorithm [4]. Assuming a homogeneous water column the psf can be calculated in the small-angle approximation. Its two-dimensional Fourier transform, the modulation transfer function, can be derived from the inherent optical properties' attenuation coefficient c and volume scattering function [5].

2.3.2. Polarization imaging. The applied Nd:YAG laser beam is characterized by a 90% linear polarization. This property may provide additional information about water column, object and background. A method for backscatter rejection next to range-gating is a polarization technique where the difference between target and background depolarization characteristics is utilized to enhance image

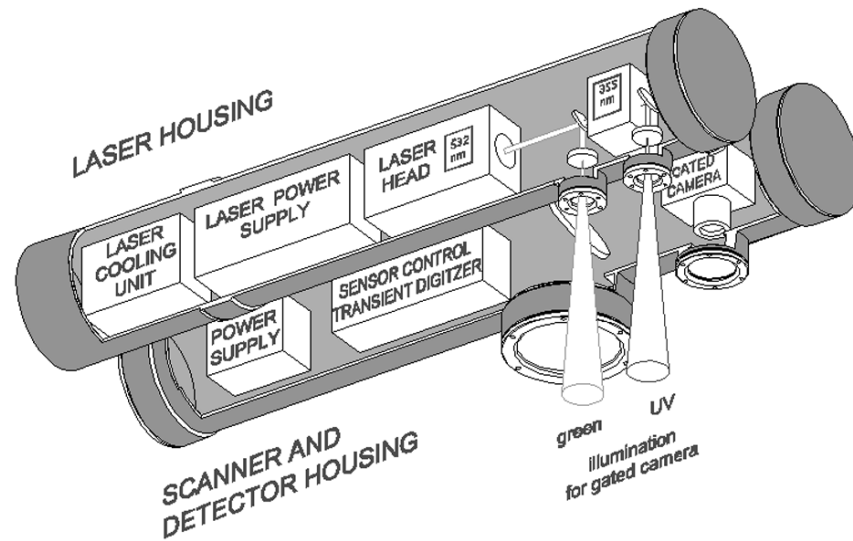


Figure 4. Schematic drawing of the submarine lidar.

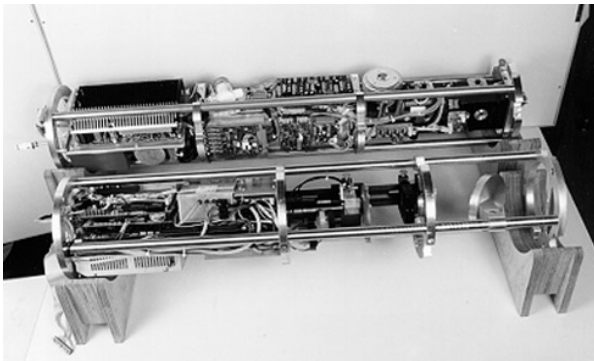


Figure 5. Laser tube and fluorescence lidar detector.

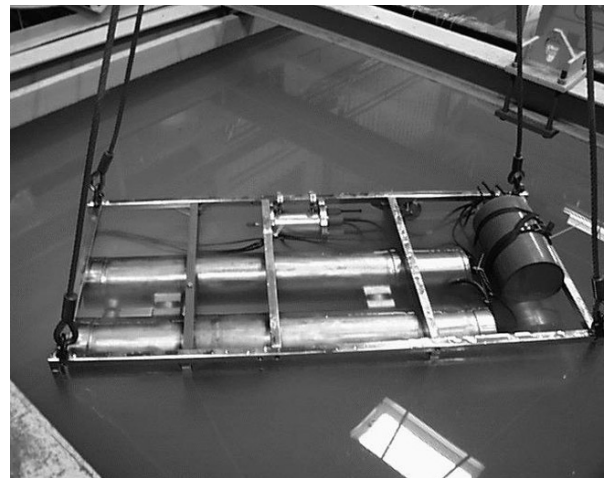


Figure 6. Tank trial of the submarine lidar.

contrast. Swartz and Cummings stated that the signal-to-noise ratio is proportional to $(C - 1)^2$, where C is the ratio of target to background reflectivities [6]. If the target and the background differ significantly in their depolarization properties, the signal-to-noise ratio of the image may increase. The same seems to be true for the signal-to-noise ratio of the image and the intervening medium as can be seen below.

Figures 9 and 10 demonstrate the advantage of the polarization method which is experimentally realized by a revolving linear polarizer in front of the camera. The polarizer can be flipped 90° to select alternatively the light parallel or perpendicular to the polarization plane of the incident laser light of a Nd:YAG laser at 532 nm. Images were recorded in a tank filled with clear seawater. Object distance is 6 m.

Figure 9 shows a laser pulse in clear ocean water illuminating a bright target with a picture of a bottle. It was recorded with a gain of 60 relative units and is comparable to a conventional video system. The position of the polarizer in front of the camera is parallel to the polarization of the incident laser beam. Due to the large amount of light backscattered by the water column in the near-field of the camera, no higher gain is possible. Figure 10 shows the



Figure 7. Scattered light image.

same image with a gain of 70 relative units and the polarizer perpendicular to the incident laser polarization. The intensity of the reflected light from the object is the same as in figure 9. This indicates that the light backscattered by the object is probably totally depolarized. The light backscattered by the water column is reduced and only a small amount is scattered back due to the partial polarization of the laser of about 90%. Therefore, a higher gain can be chosen to make use of the full

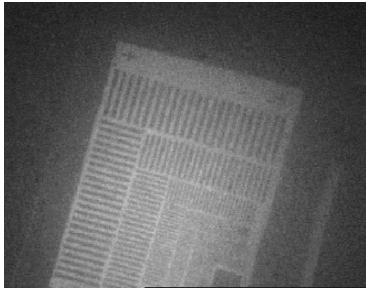


Figure 8. Range-gated image.

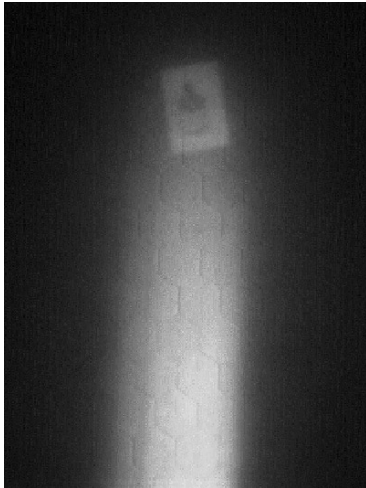


Figure 9. Parallel polarized image.



Figure 10. Perpendicular polarized image.

8 bit resolution of the CCD camera which leads to a contrast-enhanced image and which will increase the distance of target detection. Therefore, this method improves the underwater visibility, especially for video systems.

The small increase of backscattered light just in front of the object in figure 10, and also the decrease of backscattered light in the same region in figure 9, demonstrates that multiple scattering grows in clear ocean water with increasing distance. While unscattered and single scattered photons maintain the degree of incident



Figure 11. Parallel polarized image.



Figure 12. Perpendicular polarized image.

polarization, multiple scattered photons lose the information of incident polarization and carry an arbitrary polarization.

However, in many range-gating methods the polarization technique is used as an additional mechanism [7–9]. The range-gating technique is effective at backscatter rejection, and the difference between target and background depolarization characteristics is utilized to enhance image contrast. This combination is explained in figures 11 and 12. The images were recorded with a telephoto lens and a polarizer in front of the camera in the same tank with slightly increased turbidity. Object distance is 8 m.

Figure 11 shows light reflected by a metallic tin. It was recorded with a gate of 5 ns, and a gain of 85 relative units. The intensity of the light backscattered by the water column is not recorded due to the range-gating method. The position of the polarizer in front of the camera is parallel to the polarization of the incident laser beam. The high intensity of light reflected by the tin which kept the incident polarization prevents a higher gain. Figure 12 shows the image recorded under the same conditions but with a gain of 99 relative units and the polarizer perpendicular to the polarization of the incident laser pulse. The high intensity of the light reflected by the tin is rejected and only a small amount is left in the centre of the image due to the partial polarization of the laser. But now, the weak portion of light backscattered by a faint

and rough aluminium plate behind the tin is visible in the lower left corner. Due to the increase in camera sensitivity the contrast is raised over the threshold of camera resolution and is, therefore, detectable. The disadvantage is a decrease of the signal-to-noise ratio which results in a lower quality image. For both images the histogram has been numerically stretched to cover the whole range of 8 bit.

Future work will concentrate on an increase of the signal-to-noise ratio for the target and a background, e.g. the seafloor. The differential polarization method will also be investigated, which can be derived by subtracting the perpendicular polarization intensity from the parallel polarization intensity as stated by Morgan *et al* [9].

Figures 7–12 have been obtained during a tank trial of the lidar at Trondheim Marine System Large Scale Facilities. Turbidity has been produced by a phytoplankton bloom, with a maximum attenuation coefficient of 2 m^{-1} at 532 nm.

2.3.3. Fluorescence lidar measurements. Regarding a pulsed monostatic lidar, the energy $\Delta E(\lambda, R)$ collected by the detector within the wavelength interval $(\lambda, \lambda + \Delta\lambda)$ and the depth interval $(R, R + \Delta R)$ can be given in its most general form [9]

$$\begin{aligned} \Delta E(\lambda, R) &\equiv E(\lambda, R) \Delta R \Delta \lambda \\ &= \eta(\lambda) \cdot \frac{A_r}{R^2} \cdot g(R) \cdot T(\lambda, R) \cdot W(\lambda, R) \Delta R \Delta \lambda. \end{aligned} \quad (4)$$

The symbol η is the spectral transmission of the detector, and $T(\lambda, R)$ is the transmission in the medium over the range R at wavelength λ . Transmission has no physical dimension. A_r is the effective aperture of the detection optics. The ratio of A_r to R^2 describes the solid angle which is formed by the lidar detector from the distance R (in steradians). The quantity $W(\lambda, R)$ describes the energy of the induced radiation at depth R in units $\text{J sr}^{-1} \text{ m}^{-1} \text{ nm}^{-1}$. The product $W(\lambda, R) \Delta R \Delta \lambda$ is therefore the radiation induced in the depth interval $(R, R + \Delta R)$ and in the wavelength interval $(\lambda, \lambda + \Delta\lambda)$ in J sr^{-1} . The dimensionless geometrical form factor is the probability of recording a photon which is induced at a distance R and which hits the detector. Furthermore, the fundamental lidar relationship holds:

$$R = \frac{c_w \cdot t}{2}. \quad (5)$$

and hence

$$\Delta R = \frac{c_w \cdot \Delta t}{2}.$$

The factor Δt corresponds to the temporal resolution of the sensor. From equation (4) it follows that

$$\begin{aligned} E_\lambda(R) &\equiv E(\lambda, R) \Delta R \\ &= \eta(\lambda) \cdot s(R) \cdot T(\lambda, R) \cdot W(\lambda, R) \Delta R \\ &= \eta(\lambda) \cdot s(R) \cdot T(\lambda, R) \cdot W(\lambda, R) \frac{c_w \cdot \Delta t}{2} \end{aligned} \quad (6)$$

with the sensitivity function

$$s(R) := g(R) \frac{A_r}{R^2}.$$

The sensitivity function $s(R)$ has the unit sr, $E_\lambda(R)$ the unit J nm^{-1} . The transmission $T(\lambda, R)$ over distance R is

given by the attenuation coefficient $c(\lambda, R)$ and Lambert–Beer’s law

$$T(\lambda, R) = e^{-\int_0^R c(\lambda, r) dr}.$$

In the case of elastic backscattering the induced energy $W(\lambda, R)$ is determined with the approximation $R^2 \gg A_r$ by

$$W(\lambda, R) = E_l \cdot e^{-\int_0^R c_L(\lambda, L, r) dr} \cdot \beta(\pi, \lambda, R),$$

where the volume scattering function β can be interpreted as the differential cross section per volume unit, per solid angle and wavelength. E_l is the laser pulse energy. This leads to the single scattering lidar equation in a form which describes the collected energy in the time interval $(t, t + \Delta t)$:

$$\begin{aligned} E_\lambda \left(t = \frac{2R}{c_w} \right) &= \eta(\lambda_l) \cdot s(R) \cdot E_l \cdot \beta(\pi, \lambda_l, R) \\ &\cdot \frac{c_w \cdot \Delta t}{2} \cdot e^{-2 \int_0^R c(\lambda_l, r) dr}. \end{aligned} \quad (7)$$

Equation (7) implies that the laser pulse duration τ_l is much shorter than Δt . Temporal dilatations such as detector pulse response time remain unconsidered. If the average laser pulse power $P_l = E_l \tau_l$ is taken into account, the single scattering lidar equation can be written in a form which describes the radiation flux $P_\delta(\lambda, t) = E_\lambda(t) \Delta t$ detected by the receiver at time $t = 2R c_w^{-1}$ in W nm^{-1} as

$$\begin{aligned} P_\delta(\lambda_l, t) &= \eta(\lambda_l) \cdot s(R) \cdot P_l \cdot \beta(\pi, \lambda_l, R) \\ &\cdot \frac{c_w \cdot \tau_l}{2} \cdot e^{-2 \int_0^R c(\lambda_l, r) dr}. \end{aligned} \quad (8)$$

If the laser pulse duration $P_l(t)$ and pulse response function $R_r(t)$ of the detector are not much shorter than the temporal resolution Δt of the lidar, then the signal will be blurred. This means that photons induced at the same depth R are no longer detected at the same time t . Equation (5) is no longer valid. Mathematically this can be described by a convolution integral. The measured lidar signal $P(t)$ is then written as

$$P(t) = P_{\text{in}}(t) \otimes R_{\text{rn}}(t) \otimes P_\delta(t)$$

with $P_{\text{in}}(t)$ and $R_{\text{rn}}(t)$ as symbols for normalized functions of $P_l(t)$ and $R_r(t)$, respectively, and where the symbol \otimes denotes the convolution. The convolution of $P_{\text{in}}(t)$ and $R_{\text{rn}}(t)$ can be condensed to a one-system function $S_{\text{sys}}(t)$, and the convolution equation simplifies to

$$P(t) = S_{\text{sys}}(t) \otimes P_\delta(t). \quad (9)$$

The system function S_{sys} can be measured as the lidar signal of a δ -profile, e.g. a scattering, non-fluorescent surface. Deconvolution techniques can be used to extract $P_\delta(t)$ from equation (9) in the presence of noise. Equation (8) does not take into account multiple scattering effects. Monte Carlo simulations have recently shown that for a near-field lidar the intensity of the lidar return signal is significantly influenced by multiple scattering whereas its shape is not affected [11]. Inversion of the lidar equation requires complete knowledge of the lidar’s sensitivity function. The geometry of the lidar is complex so that an analytical calculation is not possible without relevant approximations. Data are therefore obtained by a Monte Carlo simulation. Figure 13 shows the results for different diameters of the diaphragm in front of the photomultiplier.

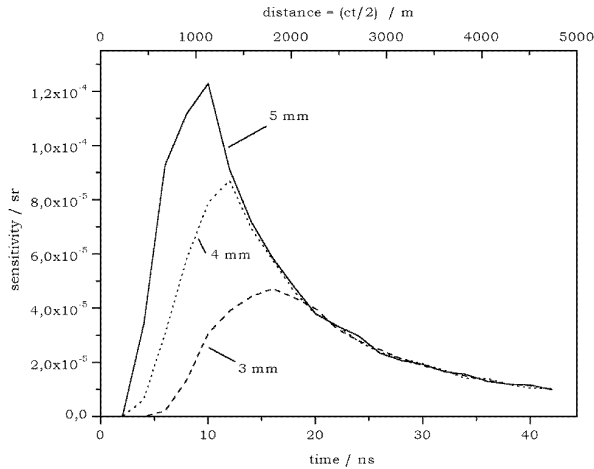


Figure 13. Sensitivity functions of the submarine lidar.

Another possibility is the direct determination of the sensitivity function by measuring the elastic backscattering in air. The signal received is proportional to the sensitivity function if the extinction coefficient is negligible. The distance, respectively time, has to be corrected by the square of the refractive index.

Inversion of a lidar signal, e.g. by the slope method, provides the two-way lidar attenuation coefficient, and the intensity at a fixed time corresponding to a certain distance gives the spectral emission, e.g. of the seafloor. Interpretation of the spectral emission allows a classification of fluorescent substances, whereas non-fluorescent but absorbing substances dissolved in the water column increase the attenuation [12].

2.4. Summary and perspectives

A prototype of the submarine lidar has been realized and successfully tested. The next step is the exact calibration of the instrument, e.g. determination of spectral sensitivity, geometrical form factor and impulse response function. Further trials will lead to a final definition of parameters like the camera's field of view and interference filters for the detection wavelength.

To improve the instrument's performance, additional techniques applying the submarine lidar will be investigated in future research. The expanded UV laser pulse as an illumination mode for the video camera is already integrated. Cut-off filters in front of the camera will lead to fluorescence images and, in the case of a fluorescent sinker, a contrast enhancement between the chemical and the seafloor. Another approach, the recording of the scattered/reflected light depolarization rate instead of its intensity, has already been preliminarily integrated and tested. Apart from its application to pollution monitoring the lidar can be used for other purposes, e.g. pipeline monitoring. With the help of

the range-gated video device an ROV can follow a pipeline in turbid waters, and the fluorescence lidar scans for oil coming from small leaks. Furthermore, applying a red-sensitive photomultiplier and a suitable interference filter chlorophyll a fluorescence at 685 nm can be detected, and the lidar can monitor the macrophytae on the seafloor.

Completion is scheduled for the end of 1999 when the German Federal Ministry of Transport intends to start the continuous operation of the submersible sensor system for the detection of chemicals in the sea.

Acknowledgments

Measurements were carried out at Trondheim Marine System Large Scale Facilities supported by the Training and Mobility of Researchers (TMR) Programme of the European Union through contract No ERBFMGECT980135. The instrument was developed with a grant of the Ministry of Research and Technology (BMBF), Germany, through the DLR Project Executive Department Environmental Protection and Technologies, Bonn.

References

- [1] VWS Versuchsanstalt für Wasserbau und Schiffbau 1992 Bekämpfung sinkender und/oder gesunkener Chemikalien *Abschlußbericht*
- [2] Gereit F, Hauptmann P, Matz G, Mellert V and Reuter R 1998 An ROV-based sensor system for maritime pollution control *Oceanology International 98 Conf. Proc. (Brighton, 1998)*
- [3] Jaffe J and Dunn C 1988 *Proc. SPIE* **925** 344–50
- [4] Ahrenberg F, Harsdorf S, Niehues J and Reuter R 1998 Contrast enhanced imaging in the sea: application of the optical transfer function for image reconstruction *EARSel Workshop on Lidar Remote Sensing of Land and Sea, Workshop Proc.* ed B Babichenko and R Reuter S 66–74
- [5] Wells W H 1969 Loss of resolution as a result of multiple small-angle scattering *J. Opt. Soc. Am.* **59** 686–91
- [6] Swartz B A and Cummings J D 1991 Laser range-gated underwater imaging including polarization discrimination *Proc. SPIE* **1537** 42–56
- [7] Demos S G and Alfano R R 1996 Temporal gating in highly scattering media by the degree of optical polarization *Opt. Lett.* **21** 161–3
- [8] Schilders S P, Gan X S and Gu M 1998 Resolution improvement in microscopic imaging through turbid media based on differential polarization gating *Appl. Opt.* **37** 4300–2
- [9] Morgan S P, Khong M P and Somekh M G 1997 Effects of polarization state and scatterer concentration on optical imaging through scattering media *Appl. Opt.* **36** 1560–5
- [10] Measures R M 1977 Lidar equation analysis allowing for target lifetime, laser pulse duration, and detector integration period *Appl. Opt.* **16** 1092–103
- [11] Harsdorf S and Reuter R 1999 *Proc. SPIE* **3821**
- [12] Mittenzwey K-H, Sinn G, Roof N and Harsdorf S 1997 An improved lidar method for monitoring surface waters: experiments in the laboratory *Int. J. Remote Sens.* **18** 2271–6